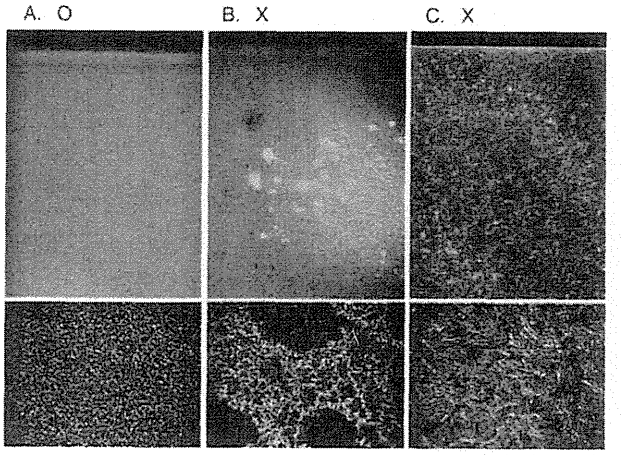

FIGURE 3.32 Result examples of DHB spray coating with the airbrush [41]. A. A properly handled spray-coating step created a uniform matrix crystal layer, and awareness of certain technical points leads to a successful coating step. B. Too small a distance between the airbrush and the tissues (<10 cm) often creates large droplets of matrix solution and results in inhomogeneous crystals. C. Humidity is also an important factor. Room humidity was held under 25% at room temperature (25°C). High humidity tends to cause formation of needle-like crystals (>80%, at room temperature). The upper panel shows stereoscopic microscope images, and the lower panel shows phase-contrast microscopic images of the matrix layer formed on the glass slides.

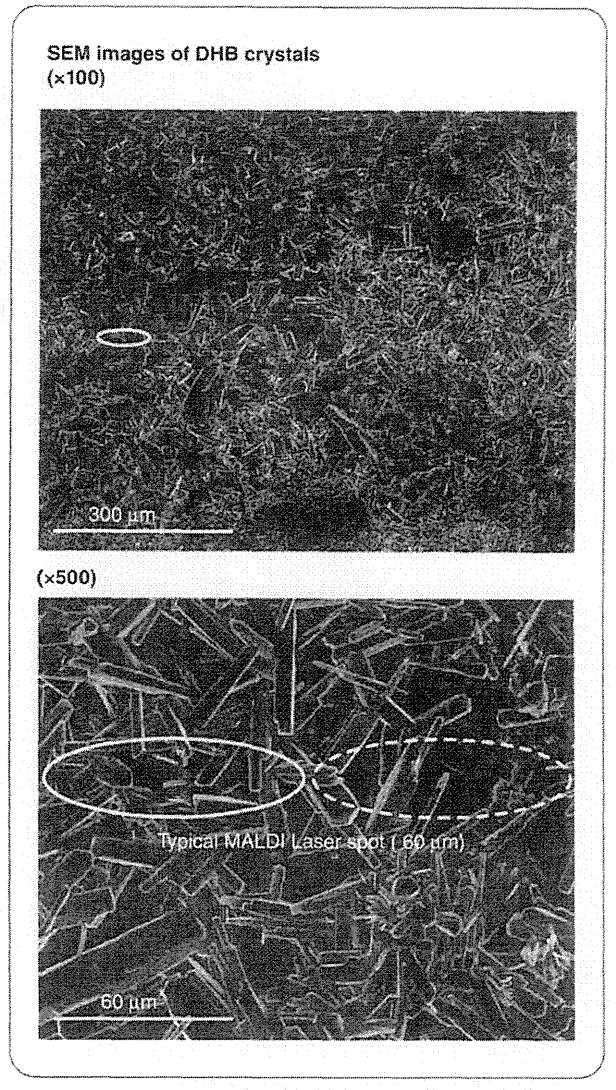

FIGURE 3.33 Size comparison of DHB crystal and typical MALDI-laser spot. DHB solution was sprayed onto the mouse brain section and the crystals were observed by SEM. The white ellipse represents the typical size of MALDI laser spot. Each matrix crystals typically have 20–60 µm length, and they did not distribute heterogeneously on the tissue surface.

and it in turn results in spot-to-spot variance of signal intensities [75,76].

This problem was at least partially solved using a spectrum-normalization procedure with total ion current (TIC) (Figure 3.33). We previously studied the effectiveness of spectrum normalization with TIC; the obtained spectra were multiplied with arbitrary variables such that all spectra had equal TIC values (i.e., equal integral values of the measured m/z region [m/z 400–900]). Such TIC normalization is available with the "Normalize Spectra" function of FlexImaging 2.0 software (Bruker Daltinics) with filter function to exclude a number of noise spectra from the normalization process (see details in the software manual).

To evaluate the effect of the normalization procedure, we prepared a section of mouse brain homogenate that had a uniform distribution of biomolecules. Figure 3.34A shows the ion images for m/z 772.6 corresponding to PC(diacyl-16:0/16:0), with and without spectrum normalization. After the normalization procedure, the image was corrected such that the ion distribution was uniform throughout the section. The signal intensity was then plotted and found to have a Gaussian distribution. Spectrum normalization with TIC improved the results of the IMS of mouse brain sections. Figure 3.34B shows the ion images of a mouse brain section for PC(diacyl-16:0/16:0), with and without spectrum normalization. In the ion image without normalization, the ion distribution was heterogeneous, even between adjacent pixels. Furthermore, the signal intensity was found to decrease with time (arrowhead). In contrast, when the normalization procedure was used, a clear ion-distribution pattern that correlated well with the anatomical features of the brain section was obtained [41].

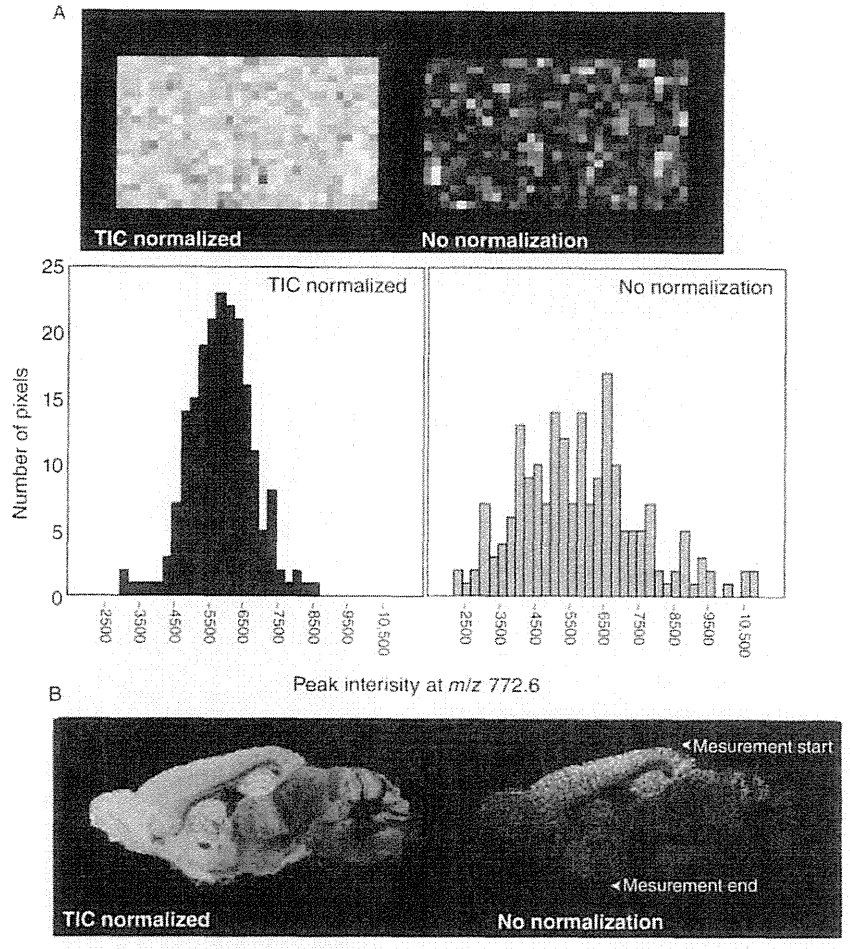

FIGURE 3.34 Spectrum normalization using TIC improves both the quantitative ability and visualization quality of IMS. A. IMS results for PC(diacyl-16:0/16:0) on a section of mouse brain homogenate, processed with or without TIC normalization (upper panel), and plot of ion intensity distribution for PC(diacyl-16:0/16:0) obtained from a brain homogenate section, with or without TIC normalization (lower panel). B. Ion images of PC(diacyl-16:0/16:0) on an adult mouse brain section, in which spectra were processed with or without TIC-normalization.

Another way of the spectrum normalization is using an external standard (ES) compound spiked in the matrix solution. We have also studied this normalization method for phospholipid imaging; the methylcarbamyl platelet-activating factor (C-PAF) (C-16) was used as the ES compound by considering the following two criteria: (1) no other mass peaks overlap the peak of the ES compound and (2) the ES compound has sufficient ionization capability on the tissue section, in which numerous biological compounds compete to ionize. All obtained spectra were multiplied to equalize the intensity of the ES and such normalization produces improved ion images of biomolecules by eliminating the variations in ionization efficiency.

First, we determined the optimal concentration of C-PAF for spectrum normalization. The spectra were normalized so that the C-PAF peaks at *m/z* 561.4 have equal intensities during the normalizing process. Figure 3.35A shows the ion images of C-PAF (*m/z* 561) with and without spectrum normalization. Regarding the brain section sprayed with the matrix solution containing 0.5, 5, and 25 mg/mL of C-PAF, spectrum normalization could not be performed successfully at some data points because of insufficient intensity of the ES peak, since mass peaks with insufficient intensity of C-PAF could not be recognized by the software as ES peaks. On the other hand, successful normalization was achieved for the section sprayed with 50 mg/mL of C-PAF, since ion signals of C-PAF equalized among the data points.

Figure 3.35B shows the ion images of PC(diacyl-16:0/18:1) (*m/z* 782) with and without spectrum normal-

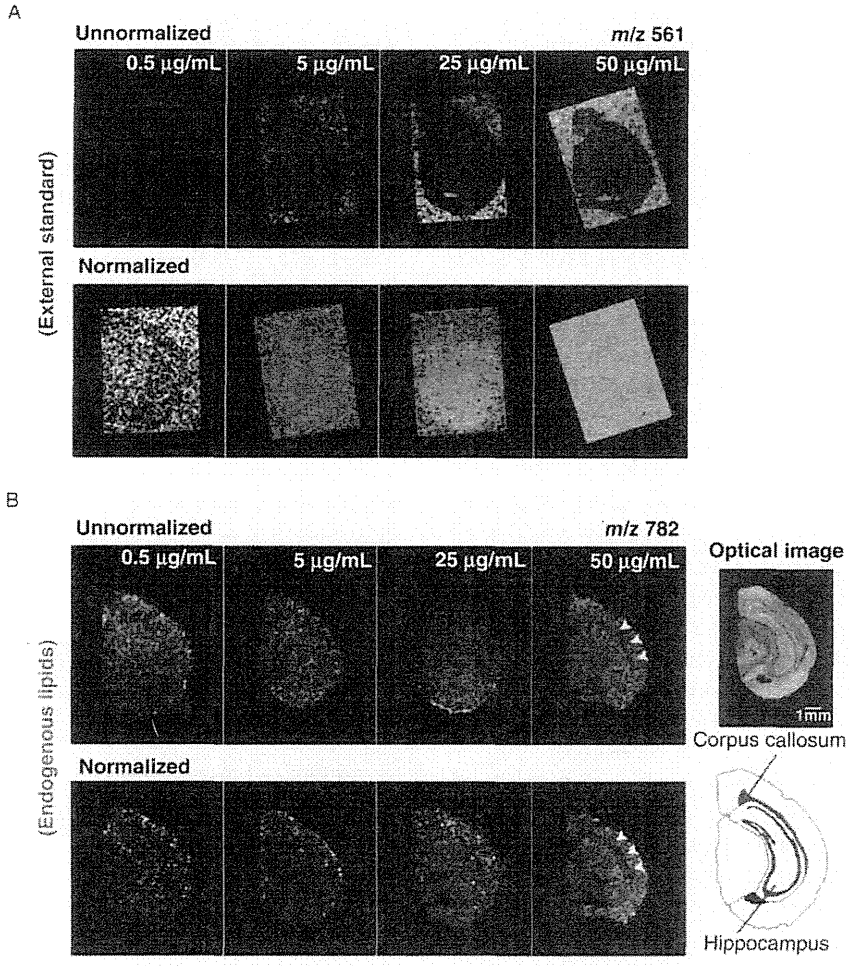

FIGURE 3.35 Comparison of unnormalized and normalized ion images. These images are successive mouse coronal brain sections. The ion at *m/z* 561 is derived from ES and *m/z* 782 is derived from PC(diacyl-16:0/18:1).

ization. While the inner structure of the brain such as the hippocampus region could not be distinguished in the unnormalized ion images, normalized images (50 mg/mL of C-PAF) showed a clear borderline of the hippocampus, indicated by the absence of PC (diacyl-16:0/18:1) in the corpus callosum (arrowheads). The normalization process with C-PAF clearly improved the ion distribution images, providing sharply defined tissue edges and increased dynamic range.

3.4 STATISTICAL PROCEDURES FOR IMS DATA ANALYSIS

3.4.1 MALDI-IMS with Statistical Analyses Revealed Abnormal Distribution of Metabolites in Colon Cancer Liver Metastasis

In the following chapter, a medical application of MALDI-IMS to colon cancer liver metastasis with use of the presented procedures is described. In addition to the shown procedures, here we employed statistical procedure for efficient analysis of complex IMS data sets. The goal of this study is to discover potential biomarkers which are specifically found in normal or diseased cells.

The IMS capability to simultaneously detect multiple metabolites at a time, even with spatial information, facilitates this emerging technique as an effective tool for biomarker discovery, within surgically resected tissues. In fact, a previous study has shown that IMS can discriminate cancer types (such as primary or nonprimary cancer) based on their molecular signature, and can even predict survival rate among human patients [77]. For this kind of purpose, it is necessary to utilize statistical analyses to extract useful information from enormous IMS data sets. The MS of tissues gives an extremely complex spectrum with hundreds of to a thousand peaks obtained from a single data point, and

furthermore, several thousands of spectra with spatial data are obtained at one IMS measurement. Because of the complexity and enormousness of the IMS data set, for discovery of biomarkers, manual processing of the data set in order to obtain significant information is not a realistic procedure. In this regard, today, multivariate analysis becomes a powerful tool in IMS data analysis. Here, we applied the statistical procedure to the IMS results of the pathological specimen, colon cancer liver metastasis.

Colon cancer is a challenging worldwide clinical problem and the incidence rate of colon cancer has been rising rapidly in Japan [78]. Genealogy is known to be a risk factor [79] and as environmental factors, aging [80] and diet, particularly a high intake of animal protein and fat along with a low intake of fiber [81], increase the incidence of colorectal cancer. Until today, a number of approaches including a cDNA microarray have revealed characteristics of cancer cells with some success, such as the discovery of specific gene expressions for drug resistance [82]. In addition to this, IMS approaches presented here which enable comprehensive analysis of metabolite expression patterns in tissues might improve our ability to understand the molecular complexities of tumor cells.

In this chapter, we will show altered composition of metabolites in the cancerous tissue revealed by IMS, with both manual data processing and statistical data management. In particular, as a statistical strategy, an unsupervised multivariate data analysis technique that enables us to sort the data sets without any reference information is described. A major method that is related to IMS, namely principal component analysis (PCA), will be described in detail.

3.4.2 Materials and Methods

3.4.2.1 Chemicals TFA was purchased from Merck (Darmstadt, Germany). Methanol was purchased from Wako Pure Chemical Industries (Osaka, Japan). 2,6-dihydroxy acetophenone (2,6-DHA) was purchased from Bruker Daltonics. A calibration standard for the low m/z region was prepared by mixing angiotensin III ($[M+H]^+$: 899.47) and Leu-Euk ($[M+H]^+$: 556.28). All the chemicals used in this study were of the highest purity available.

3.4.2.2 Conductive Sheet The conductive sheet was purchased from Tobi Co., Ltd. (Osaka, Japan). This sheet has a thin ITO layer on a polyethylene terephthalate. The sheet was 125 μm thick and its conductivity was 100 Ω. The transparency was 80% ($\lambda = 550$ nm), so that we could observe stained tissues with transmitted light. This flexible sheet made sample handling easy, because the sheet could be cut to an arbitrary size with a paper cutter and samples did not crack easily, which was sometimes problematic with glass slides.

3.4.2.3 Tissue Block Preparation A tissue block with colon cancer liver metastasis was removed from a Japanese patient during an operation, and rinsed with PBS buffer. The tissue was then immediately frozen in liquid nitrogen to minimize degradation, and was kept at −80°C. Informed consent was obtained before the operation.

3.4.2.4 Sample Preparation Before sectioning, the liver block was left for 30 min at −20°C. The tissue sections were sliced to a thickness of 3 μm using a cryostat (CM 3050; Leica) and mounted onto the ITO sheet. A thin matrix layer was applied to the surface by an airbrush. A 2-min spraying of 2,6-DHA solution (30 mg/mL in 70% methanol/0.1% TFA) was iterated twice. During spraying, the distance between the nozzle and the tissue surface was kept at 15 cm. After drying, the ITO sheet was attached to a metal-coated glass slide by conductive tape to facilitate electrical conduction.

3.4.2.5 Conditions of MS and MALDI-IMS The tissue section was analyzed using a matrix-assisted laser desorption/ionization time-of-flight mass spectrometry (MALDI-TOF)/time of flight (TOF)-type instrument, Ultraflex II TOF/TOF (Bruker Daltonics), which was equipped with a Nd:YAG laser with a 200 Hz repetition rate. External calibration solution was deposited on the surface of the ITO sheet to minimize mass shift. In this experiment, an acceleration voltage was set to 25 kV.

3.4.2.6 IMS A raster scan on the tissue surface was performed automatically. Laser irradiation consisted of 100 shots in each spot. The interval of data points was 100 μm, giving a total of 445 data points in the tissue section. The spectra shown in the results section were accumulated in square sections (300 × 300 μm) of normal and cancerous areas. Here, we did not apply data processing such as smoothing or baseline subtraction. The reconstructions from the spectra were performed by FlexImaging (Bruker Daltonics).

3.4.2.7 Statistical Analysis Statistical analyses were carried out using the ClinProTools 2.2 Software (Bruker Daltonics). For the statistical analyses, the mass spectra were internally recalibrated on common peaks (also known as spectral alignment) and normalized on the TIC. An average spectrum created from all single spectra was used for a peak picking and to define integration ranges. These integration ranges were used to

obtain the intensities or areas on the single spectra. The signal intensities were used for all calculations.

3.4.3 Results and Discussion

3.4.3.1 Comparison of Averaged Mass Spectra in Normal and Cancerous Areas At first, a tissue section with colon cancer liver metastasis was stained with HE for histological observation (Figure 3.36a). The histochemical staining enables us to distinguish the normal, stroma, and cancer cells which were localized on the left, middle, and right locations of the tissue section, respectively. A successive tissue section was used for MALDI-IMS and after the measurement, according to the histological observation, two quadrate areas—one from the normal area and the other from the cancerous area—were selected to collect and average the obtained mass spectra (Figure 3.36b).

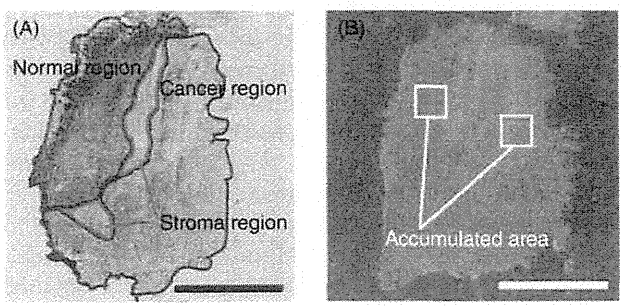

FIGURE 3.36 Histological observation of HE-stained liver tissue section with colon cancer metastasis. A. The HE-stained section allows us to distinguish the normal, stroma, and cancer cells which were localized on the left, middle, and right locations of the section, respectively. B. Photograph of the tissue section prepared for MALDI-IMS. From the data points in white squares represented in B, mass spectra were collected and averaged. Bars: 1 mm.

Figure 3.37 shows the averaged mass spectra from the cancerous (Figure 3.37a) and normal area (Figure 3.37b). Numerous differences on the mass signals were observed between the normal and cancerous cells. In particular, we found that the signal at m/z 725 showed a massive increase in the cancerous region while the ion at m/z 616 almost disappeared in the cancer cells.

3.4.3.2 Visualization of Molecules Specifically Localized in Normal and Cancerous Region Having demonstrated the cancerous/normal tissue specific localization of ions at m/z 616 and 725, respectively, we proceed to the visualization of their distribution pattern. As expected, the ion distribution images shown in Figure 3.38 demonstrate that they are expressed in the normal/diseased region specific manner: ion at m/z 725 was clearly localized in the cancerous region while ion at m/z 616 was found only in the normal cell region. The merged image demonstrates that these two ions were complementarily distributed in the specimen.

3.4.3.3 Molecular Identification with MS/MS Next question is the origin of these two ions. As shown in previous chapters, MS/MS provides the structural information of interest ions and therefore, it enables the molecular identification. The result of MS/MS with regard to m/z 725 is shown in Figure 3.39A. In the product ion mass spectrum, peaks at m/z 666.5 and 542.5, which correspond to neutral loss (NL) of trimethylamine (59 u, C_3H_9N) and NL of trimethylamine and cyclophosphate (124 u, $C_2H_5O_4P$), respectively, were detected. This result indicates that m/z 725 contained an alkali metal adduct phosphocholine, therefore ion at m/z 725 is suggested to be PC or sphingomyelin (SM) [41]. According to the nitrogen rule, ion at m/z 725 having odd nominal mass should contain additional nitrogen in its structure, thus indicating presence of a sphingosine. We concluded that m/z 725 was attributed to be a sodiated molecule of SM (16:0).

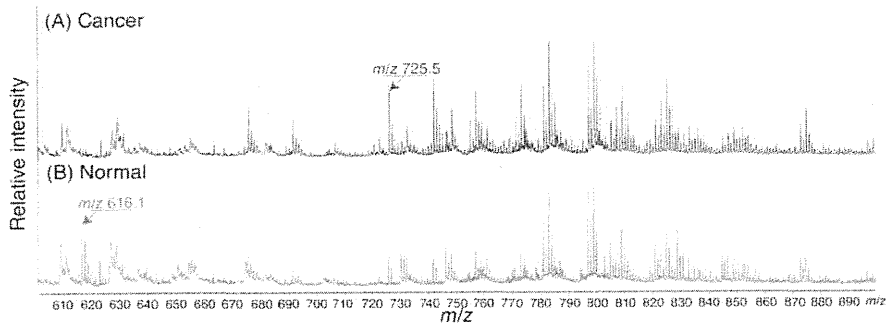

FIGURE 3.37 Comparison of averaged mass spectra from the (A) cancerous and (B) normal areas.

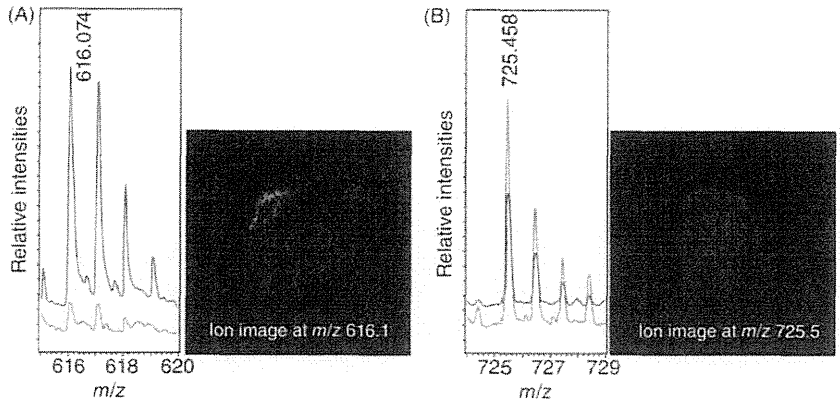

FIGURE 3.38 Visualization of molecules specifically localized in normal and cancerous region. Ion distribution images and corresponding mass spectra demonstrate the strong distribution of ion at *m/z* 616 in the normal area (A), while the ion at *m/z* 725 showed higher expression in the cancerous area than in the normal area (B).

Regarding the ion at *m/z* 616, the first generation of product ion mass spectrum from *m/z* 616 showed consecutive NLs of 73, 59, and 45 Da (Figure 3.39B[a]). From the previous literature [83,84], it is suggested that *m/z* 616 corresponded to heme B and that these NLs were derived from loss of the CH2CH2COOH (73 Da), CH2COOH (59 Da), or the COOH (45 Da) group, respectively. The molecular structure of heme B is displayed as an inset. Figure 3.39B(b) shows the second product ion mass spectrum generated from *m/z* 557, and an additional NL of 59 Da was observed. This fragment was considered to be derived from another CH2COOH in heme B.

Here, we demonstrate that SM(16:0) was strongly expressed in the cancerous area. Previous studies reported that in colon cancer, the cancerous cells contain elevated amounts of total phospholipids [85], and in addition, the phospholipid composition of the cellular membrane is altered [85,86] even between cancer cell types, that is, metastases and nonmetastatic cancer [86]. Brasitus et al. studied a relationship between the malignancy and altered lipid composition of the colon cancer, and reported significant accumulation of SM, consistent with the presented result [87]. On the other hand, heme B consists of an iron atom and porphyrin, and is known as a prosthetic group in hemoglobin, which is a protein in erythrocytes. Presented results indicate the difference between the blood-rich organ liver and the ischemic metastatic colon cancer [88,89].

3.4.3.4 IMS Linked to Multivariate Analysis Up to this point, we showed that two small metabolites were specifically expressed between the cancerous and normal tissue areas. In the described data analysis procedures without statistical methods, we usually averaged the spectra of each region and visually compared the mass peaks between the spectra one by one. As seen in Figure 3.37, with such visual comparisons of spectra, we were certainly able to find differences among the peak expressions. However, such methodology is inefficient especially when one is analyzing a large number of mass peaks and/or many tissue samples.

Below, we will describe the IMS-linked PCA to compare the metabolite composition of the normal/cancerous regions. Here, we will not describe the detailed mathematical theory due to the space limitation, but in brief, PCA is a statistical method that merges the data containing multiple elements into low-dimensional data. It reduces a large set of variables to a small set of variables called "principal components" which are linear combinations of the original variables. In the PCA-coupled IMS data analysis, spectra obtained by IMS are processed to peak detection and based on the generated peak list, PCA decomposition was performed. PCA images (i.e., 2D intensity map of principle component score on the tissue section) were often utilized to find differences of molecular composition among regions/tissues.

PCA calculation results in several parameters and below, the *component score* and *factor loading* are particularly important for the interpretation of results. A component score is calculated for each mass spectrum; all are defined for each principal component (e.g., for PC1, PC2, etc.). Those component scores are often plotted two-dimensionally, to facilitate interpretation of the PCA results. In Figure 3.40, component scores for each principle component are plotted on the *x*- and *y*-axis, and each dot in the graph represents a spectrum

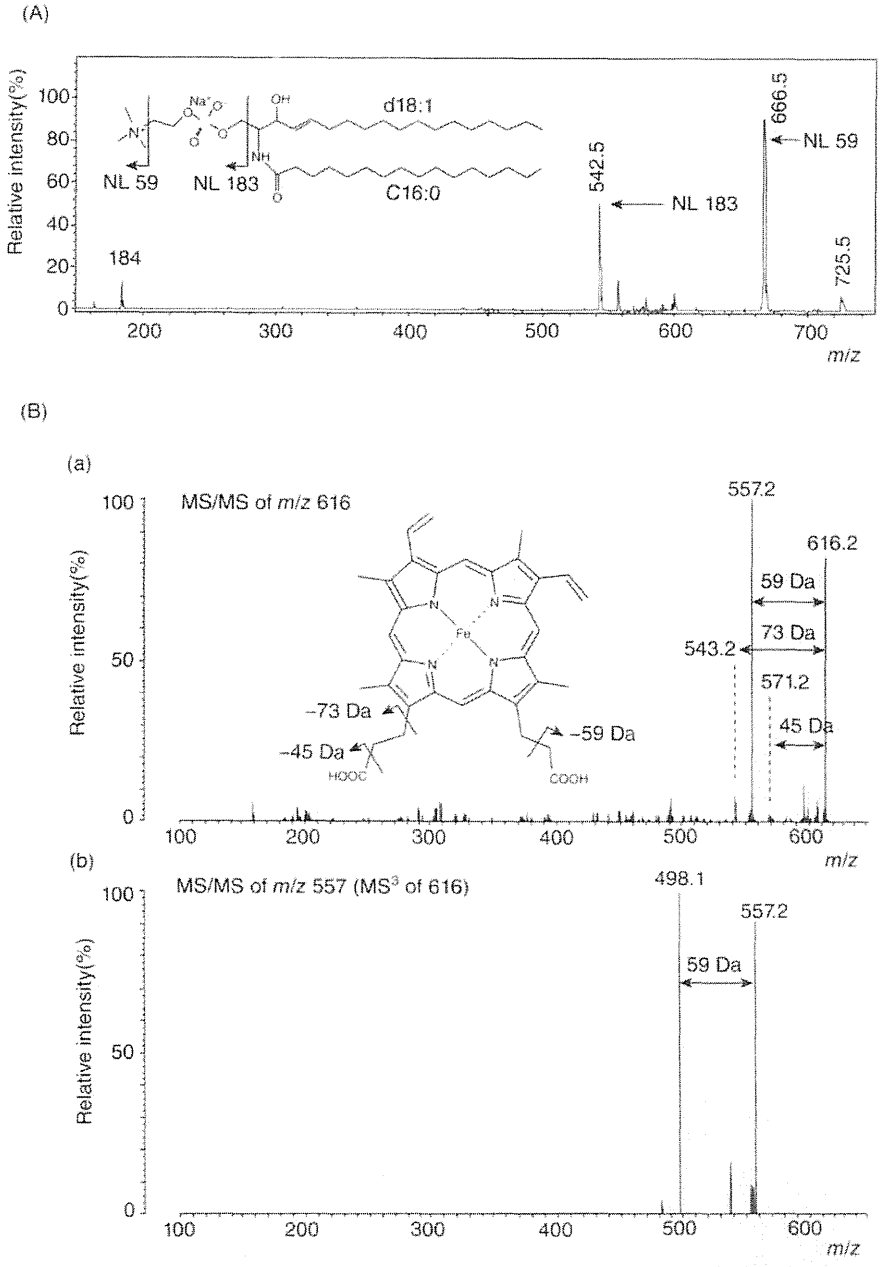

FIGURE 3.39 MS/MS enables the molecular identification of interested ions directly on the tissue surface. A. Product ion mass spectrum on the liver section of *m/z* 725. The NL of 59 and 124 u observed in the spectra is trimethylamine and cyclophosphate, indicating phosphocholine structure. This fragmentation occurred when alkali metal adducted to the precursor ion. The biomolecule of *m/z* 725 was suggested to be the sodiated molecule of SM(16:0). B. Product ion mass spectra on the liver section of *m/z* 616.2 (a) and 557.2 (b). The *m/z* value and fragment patterns indicate that the product ion of *m/z* 616 is heme B. Consecutive NLs of 73, 59, and 45 Da correspond to CH2CH2COOH, CH2COOH, and COOH, respectively. The molecular structure of heme B is shown as an inset in (a).

from a distinct data point on the tissue section. What is important to note is whether two (or several) populations of spectra (= dot) are obtained from distinct regions, for example, normal versus diseased, they are spatially separated on the graph, or not. If they are separated (Figure 3.40A), it means that the molecular expression patterns of these two regions were statistically distinct from each other. If not, PCA failed to extract the statistical differences between the populations (Figure 3.40B).

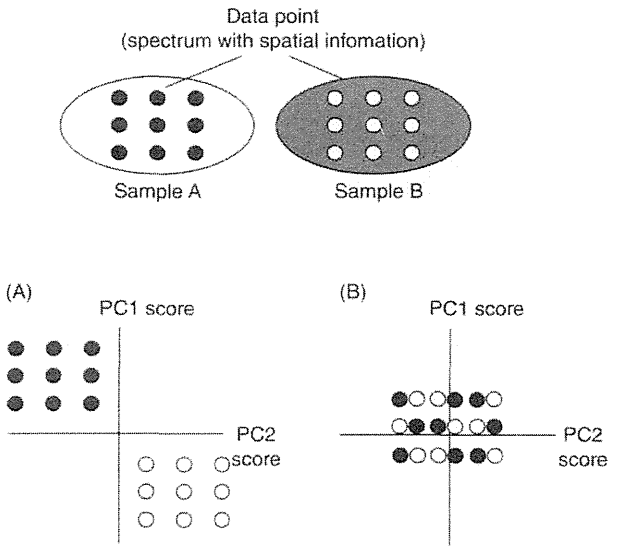

FIGURE 3.40 Example of data interpretation of IMS-linked PCA. In this study, dots seen in the 2D plot represent the *case*, that is, the spectrum from distinct data points. If dots from distinct sample are separated (A), it means that the molecular expression patterns of these two regions were statistically distinct from each other. If not, PCA failed to extract the statistical differences between the two populations (B).

Figure 3.41 shows the result of imaging mass spectrometry–principal component analysis (IMS-PCA) for the colon cancer tissue. In this case, this unsupervised analysis revealed that the largest spectral difference (i.e., the largest difference in metabolite composition) was observed between the normal and the other tissue areas (i.e., normal vs. stroma/cancer area), and the second largest difference was observed between the stroma and normal/cancer area. The overall interpretation of PCA was shown in Table 3.6.

In the graphs shown in Figure 3.41B, the circles indicate mass spectra obtained from the normal, stroma, and cancerous regions (colored white, gray, and black, respectively). Notably, the three populations are spatially separated by the component scores for PC2 and PC3, but not for PC1. This indicates that PC2 and PC3 particularly contain the statistical differences among these three regions.

In detail, along with the PC2 scores (x-axis), the spectra from normal and the others are clearly separated. The PC2 image also demonstrates a large difference of PC2 score value between normal and the other regions (Figure 3.41C). On the other hand, along with the PC3 scores (y-axis), spectra from stroma and the other regions are separated and the PC3 image also shows much higher PC3 score value of stroma region than the other regions (Figure 3.41C).

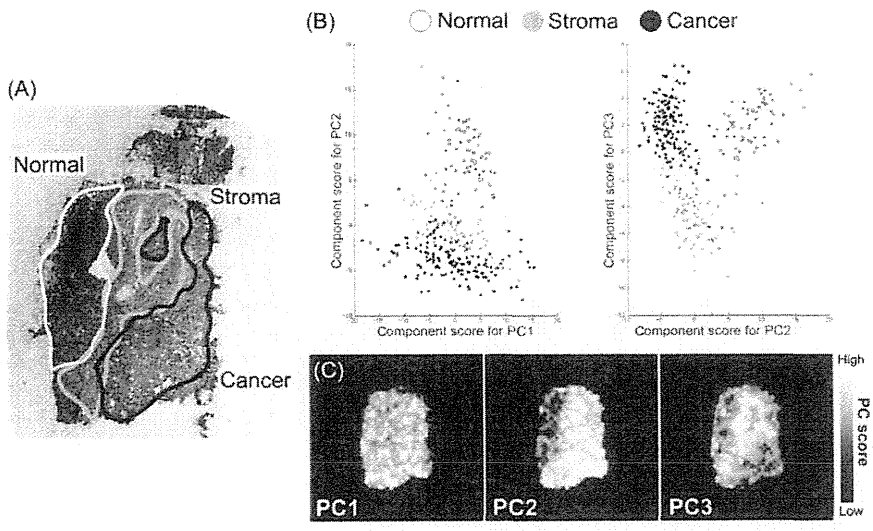

FIGURE 3.41 IMS-linked PCA of colon cancer liver metastasis section revealed altered metabolite compositions among normal stroma and cancer regions. A. Optical images of HE-stained section after IMS measurement representing the normal, stroma, and cancer regions. B. Graphs in which principle component scores for PC1, PC2, and PC3 are plotted. C. Principal component images. According to the value of the principle component score calculated for the spectrum at each tissue location, pixels are indicated with gray value.

TABLE 3.6 The Results and Interpretation of PCA of the Liver Section with Colon Cancer Metastasis

		Primary Contributing PCs			Interpretation of the Component
Component 2	Negative	*m/z* 616.2 (heme B)	*m/z* 828.4 c/t [PC(diacyl-16:0/22:6)+Na]$^+$)	*m/z* 844.4 c/t [PC(diacyl-16:0/22:6)+Na]$^+$)	Representing altered metabolite composition between normal and other regions.
	Positive	*m/z* 744.4	*m/z* 754.4	*m/z* 768.4	
Component 3	Negative	*m/z* 722.0	–	–	Representing altered metabolite composition between stroma and other regions.
	Positive	*m/z* 760.4	*m/z* 766.4		

3.4.3.5 Analysis of Loading Factor for Each Principle Component Facilitates Identification of "Responsible" Molecules Which Differentiate Control and Diseased Samples As a next step, an analysis of the factor loading plot would identify peaks that were differentially expressed between regions. Since a component score defined for each spectrum is a sum of the value of the factor loading value, multiplied by peak intensity, when numbers (= m) of mass peaks were used in the analysis, the component score will be:

$$\text{ScorePC1}(x,y) = \sum_{n=1}^{m} \text{load}(n) \times \text{Int.}(n),$$

where

ScorePC1(x,y) = component score against PC1, obtained from (x, y).
load(n) = factor loading value against a mass peak for n.
Int.(n) = mass peak intensity for n.
m = number of mass peaks used for calculation.

According to this equation, in the spectra from the normal tissue region, the mass peak with large negative value regarding PC2 factor loading is supposed to be intense. On the other hand, it was also indicated that peaks with large positive values for PC2 factor loading would be specific molecules to the stroma/cancerous regions. In other words, such mass peaks with a radical absolute value for PC2 factor loading are suggested to be major contributors to differentiate these regions.

3.4.3.6 PC2 Represents Difference of Metabolite Composition between Normal versus Other Region In Figure 3.42, the factor loading values for PC1 and PC2 are plotted on the x- and y-axes, respectively. Each dot indicates a distinct mass peak. Such a graph makes it very easy to find the peaks with the intended factor loading value against each PC. Since peaks that have negative loading values regarding PC2 are supposed to be specifically expressed by the normal liver cells, we thus picked up mass peaks with large negative loading values for PC2, and obtained their distribution image. As a result, we found that ion at *m/z* 616.2, which is already demonstrated as a normal region-specific molecule, was statistically classified into the *normal region specific* category (Figure 3.42, lower part). Furthermore, by this procedure, other mass peaks corresponding to sodiated and potassiated molecules of PC(diacyl-16:0/22:6) were identified as the normal cell specific metabolites (Figure 3.42, lower part). On the other hand, through the same procedure, we also successfully identified the molecules which localized in the cancerous/stroma region (Figure 3.42, upper part).

3.4.3.7 PC3 Represents Difference of Metabolite Composition between Stroma versus Other Region In Figure 3.43, the factor loading values for PC1 and PC3 are plotted on the x- and y-axes, respectively. In this case, since mass peaks that have a large positive loading value regarding PC3 are supposed to be specific molecules to the stroma region, we picked up the mass peak at *m/z* 722.0 and obtained a distribution image (Figure 3.43, upper part). As a result, we identified ions at *m/z* 722.0 as stroma-specific molecules, and on the other hand, with same procedure, we revealed that ions at *m/z* 760.4 and 766.4 almost disappeared in the stroma region.

3.4.4 Conclusion

Biomarkers are objective indicators of particular pathogenic processes, pharmacological responses, or normal biological states; they can involve any kind of molecule in living organs, for example, proteins, peptides, DNA, and/or metabolites. Biomarkers are essential for the diagnosis and prediction of diseases; IMS can provide distribution information regarding various biomolecules at the cell and tissue levels, and thus it is expected to become a powerful tool for in situ biomarker discovery.

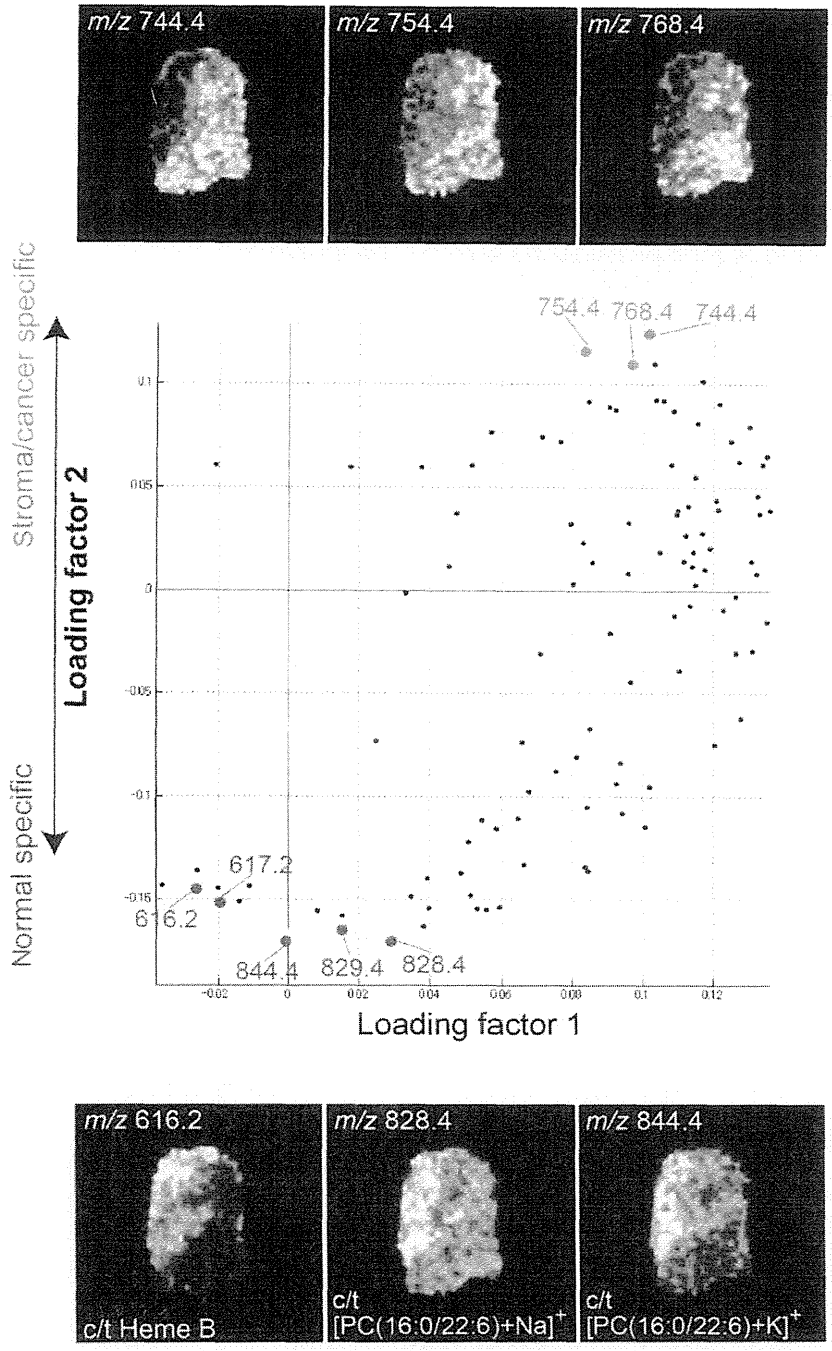

FIGURE 3.42 PC2 represents difference of metabolic composition between normal and other region. In the center graph, factor loading values for PC1 and PC2 are plotted on the *x*- and *y*-axes, respectively. Each dot indicates the distinct mass peak. The peaks with a large positive/negative value for loading factor 2 (i.e., major contributors to differentiation among the groups) were chosen and their distribution images are visualized. c/t, corresponding to.

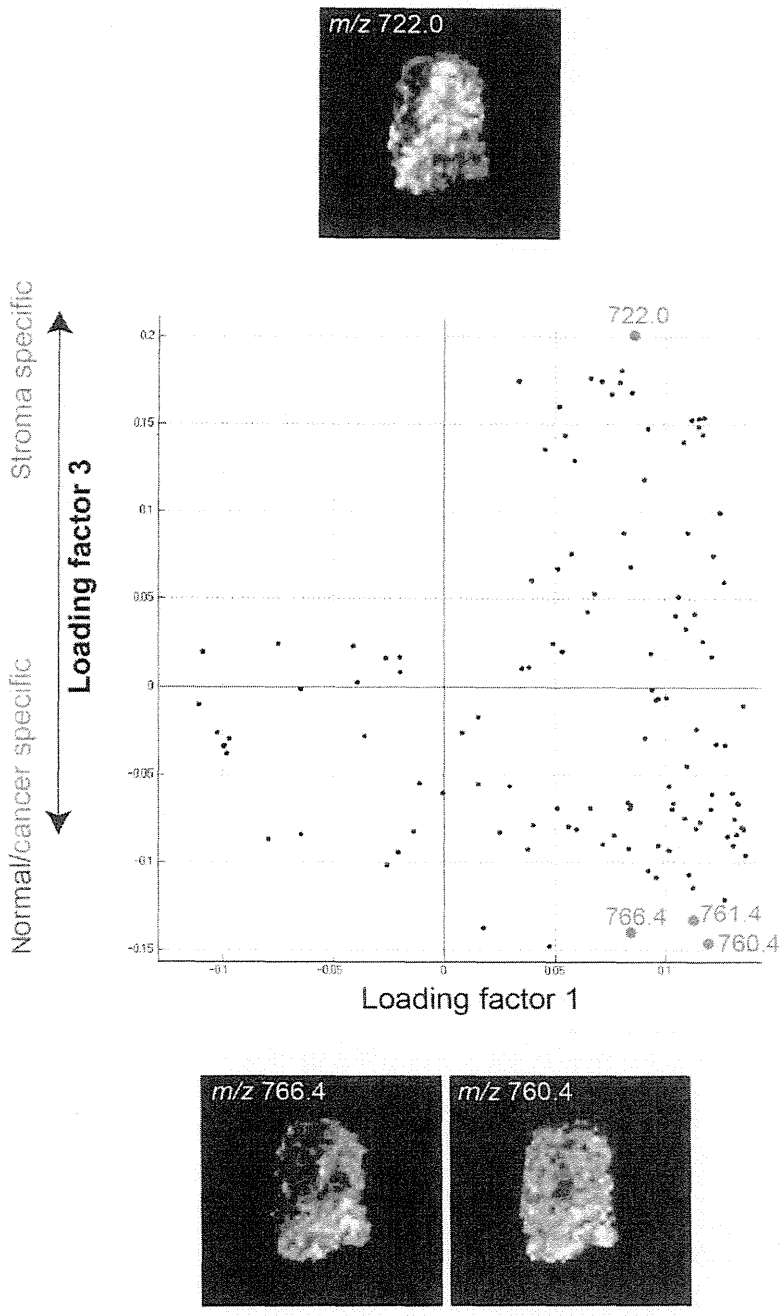

FIGURE 3.43 PC2 represents difference of metabolic composition between normal versus other region. In the center graph, factor loading values for PC1 and PC3 are plotted on the *x*- and *y*-axes, respectively. The mass peaks with large positive/negative value for loading factor 3 were chosen and their distribution images are visualized.

In this chapter, we showed the identification of potential biomarkers, which are molecules that differentiate among the normal, cancerous and even stroma cells in the colon cancer liver metastasis. For this purpose, we showed that the statistical strategy is quite effective to deal with the large volume data set of IMS.

The volumes of IMS data sets continue to increase because of current improvements to IMS with regards to high-resolution [90], three-dimensional (3D) imaging [71], and reconstruction from 3D mass spectra containing ion drift times in ion mobility MS [29]. Data analysis of such large data sets will increasingly depend on the statistical analysis, and therefore the development and application of such analyses will be a more important issue.

REFERENCES

1. Garrett, T.J., et al. (2006) Imaging of small molecules in tissue sections with a new intermediate-pressure MALDI linear ion trap mass spectrometer. *International Journal of Mass Spectrometry*, *260*, 11.
2. Khatib-Shahidi, S., Andersson, M., Herman, J.L., Gillespie, T.A., Caprioli, R.M. (2006) Direct molecular analysis of whole-body animal tissue sections by imaging MALDI mass spectrometry. *Analytical Chemistry*, *78*, 6448–6456.
3. Stoeckli, M., Staab, D., Staufenbiel, M., Wiederhold, K.H., Signor, L. (2002) Molecular imaging of amyloid beta peptides in mouse brain sections using mass spectrometry. *Analytical Biochemistry*, *311*, 33–39.
4. Chaurand, P., Norris, J.L., Cornett, D.S., Mobley, J.A., Caprioli, R.M. (2006) New developments in profiling and imaging of proteins from tissue sections by MALDI mass spectrometry. *Journal of Proteome Research*, *5*, 2889–2900.
5. Krause, E., Wenschuh, H., Jungblut, P.R. (1999) The dominance of arginine-containing peptides in MALDI-derived tryptic mass fingerprints of proteins. *Analytical Chemistry*, *71*, 4160–4165.
6. Gharahdaghi, F., Kirchner, M., Fernandez, J., Mische, S.M. (1996) Peptide-mass profiles of polyvinylidene difluoride-bound proteins by matrix-assisted laser desorption/ionization time-of-flight mass spectrometry in the presence of nonionic detergents. *Analytical Biochemistry*, *233*, 94–99.
7. Annesley, T.M. (2003) Ion suppression in mass spectrometry. *Clinical Chemistry*, *49*, 1041–1044.
8. Jones, J.J., Borgmann, S., Wilkins, C.L., O'Brien, R.M. (2006) Characterizing the phospholipid profiles in mammalian tissues by MALDI FTMS. *Analytical Chemistry*, *78*, 3062–3071.
9. Lemaire, R., et al. (2006) MALDI-MS direct tissue analysis of proteins: Improving signal sensitivity using organic treatments. *Analytical Chemistry*, *78*, 7145–7153.
10. Schwartz, S.A., Reyzer, M.L., Caprioli, R.M. (2003) Direct tissue analysis using matrix-assisted laser desorption/ionization mass spectrometry: practical aspects of sample preparation. *Journal of Mass Spectrometry*, *38*, 699–708.
11. Seeley, E.H., Oppenheimer, S.R., Mi, D., Chaurand, P., Caprioli, R.M. (2008) Enhancement of protein sensitivity for MALDI imaging mass spectrometry after chemical treatment of tissue sections. *Journal of the American Society for Mass Spectrometry*, *19*, 1069–1077.
12. Mann, M., Jensen, O.N. (2003) Proteomic analysis of post-translational modifications. *Nature Biotechnology*, *21*, 255–261.
13. Yan, R., et al. (1999) Membrane-anchored aspartyl protease with Alzheimer's disease beta-secretase activity. *Nature*, *402*, 533–537.
14. Rohner, T.C., Staab, D., Stoeckli, M. (2005) MALDI mass spectrometric imaging of biological tissue sections. *Mechanisms of Ageing and Development*, *126*, 177–185.
15. McDonnell, L.A., Heeren, R.M. (2007) Imaging mass spectrometry. *Mass Spectrometry Reviews*, *26*, 606–643.
16. Groseclose, M.R., Andersson, M., Hardesty, W.M., Caprioli, R.M. (2007) Identification of proteins directly from tissue: in situ tryptic digestions coupled with imaging mass spectrometry. *Journal of Mass Spectrometry*, *42*, 254–262.
17. Shimma, S., Furuta, M., Ichimura, K., Yoshida, Y., Setou, M. (2006) A novel approach to in situ proteome analysis using chemical inkjet printing technology and MALDI-QIT-TOF tandem mass spectrometer. *Journal of the Mass Spectrometry Society of Japan*, *54*, 133–140.
18. Shimma, S., et al. (2008) Mass imaging and identification of biomolecules with MALDI-QIT-TOF-based system. *Analytical Chemistry*, *80*, 878–885.
19. Setou, M., Hayasaka, T., Shimma, S., Sugiura, Y., Matsumoto, M. (2008) Protein denaturation improves enzymatic digestion efficiency for direct tissue analysis using mass spectrometry. *Applied Surface Science*, *255*, 1555–1559.
20. Woo, H.K., Northen, T.R., Yanes, O., Siuzdak, G. (2008) Nanostructure-initiator mass spectrometry: a protocol for preparing and applying NIMS surfaces for high-sensitivity mass analysis. *Nature Protocols*, *3*, 1341–1349.
21. Patti, G.J., et al. (2010) Detection of carbohydrates and steroids by cation-enhanced nanostructure-initiator mass spectrometry (NIMS) for biofluid analysis and tissue imaging. *Analytical Chemistry*, *82*, 121–128.
22. Liu, Q., Guo, Z., He, L. (2007) Mass spectrometry imaging of small molecules using desorption/ionization on silicon. *Analytical Chemistry*, *79*, 3535–3541.
23. Taira, S., et al. (2008) Nanoparticle-assisted laser desorption/ionization based mass imaging with cellular resolution. *Analytical Chemistry*, *80*, 4761–4766.
24. Harada, T., et al. (2009) Visualization of volatile substances in different organelles with an atmospheric-pressure mass microscope. *Analytical Chemistry*, *81*, 9153–9157.
25. Holscher, D., et al. (2009) Matrix-free UV-laser desorption/ionization (LDI) mass spectrometric imaging at the single-cell level: distribution of secondary metabolites of

Arabidopsis thaliana and Hypericum species. *The Plant Journal*, *60*, 907–918.

26. Jackson, S.N., Wang, H.Y., Woods, A.S. (2005) In situ structural characterization of phosphatidylcholines in brain tissue using MALDI-MS/MS. *Journal of the American Society for Mass Spectrometry*, *16*, 2052–2056.
27. Jackson, S.N., Wang, H.Y., Woods, A.S. (2007) In situ structural characterization of glycerophospholipids and sulfatides in brain tissue using MALDI-MS/MS. *Journal of the American Society for Mass Spectrometry*, *18*, 17–26.
28. Rujoi, M., Estrada, R., Yappert, M.C. (2004) In situ MALDI-TOF MS regional analysis of neutral phospholipids in lens tissue. *Analytical Chemistry*, *76*, 1657–1663.
29. McLean, J.A., Ridenour, W.B., Caprioli, R.M. (2007) Profiling and imaging of tissues by imaging ion mobility-mass spectrometry. *Journal of Mass Spectrometry*, *42*, 1099–1105.
30. Sugiura, Y., Setou, M. (2009) Imaging mass spectrometry for visualization of drug and endogenous metabolite distribution: toward in situ pharmacometabolomes. *Journal of Neuroimmune Pharmacology*, *5*, 31–43.
31. Wang, H.Y., Jackson, S.N., Woods, A.S. (2007) Direct MALDI-MS analysis of cardiolipin from rat organs sections. *Journal of the American Society for Mass Spectrometry*, *18*, 567–577.
32. Sugiura, Y., Setou, M. (2009) Selective imaging of positively charged polar and nonpolar lipids by optimizing matrix solution composition. *Rapid Communications in Mass Spectrometry*, *23*, 3269–3278.
33. Han, X., Gross, R.W. (2001) Quantitative analysis and molecular species fingerprinting of triacylglyceride molecular species directly from lipid extracts of biological samples by electrospray ionization tandem mass spectrometry. *Analytical Biochemistry*, *295*, 88–100.
34. Hsu, F.F., Turk, J. (2001) Structural determination of glycosphingolipids as lithiated adducts by electrospray ionization mass spectrometry using low-energy collisional-activated dissociation on a triple stage quadrupole instrument. *Journal of the American Society for Mass Spectrometry*, *12*, 61–79.
35. Piomelli, D., Astarita, G., Rapaka, R. (2007) A neuroscientist's guide to lipidomics. *Nature Reviews. Neuroscience*, *8*, 743–754.
36. Hitzemann, R.J., Johnson, D.A. (1983) Developmental changes in synaptic membrane lipid composition and fluidity. *Neurochemical Research*, *8*, 121–131.
37. Zerouga, M., Jenski, L.J., Stillwell, W. (1995) Comparison of phosphatidylcholines containing one or two docosahexaenoic acyl chains on properties of phospholipid monolayers and bilayers. *Biochimica et Biophysica Acta*, *1236*, 266–272.
38. Ostrowski, S.G., Van Bell, C.T., Winograd, N., Ewing, A.G. (2004) Mass spectrometric imaging of highly curved membranes during Tetrahymena mating. *Science*, *305*, 71–73.
39. Murakami, M., Nakatani, Y., Atsumi, G., Inoue, K., Kudo, I. (1997) Regulatory functions of phospholipase A2. *Critical Reviews in Immunology*, *17*, 225–283.
40. Astarita, G., Ahmed, F., Piomelli, D. (2008) Identification of biosynthetic precursors for the endocannabinoid anandamide in the rat brain. *Journal of Lipid Research*, *49*, 48–57.
41. Sugiura, Y., et al. (2009) Visualization of the cell-selective distribution of PUFA-containing phosphatidylcholines in mouse brain by imaging mass spectrometry. *Journal of Lipid Research*, *50*, 1776–1788.
42. Salem, N., Jr., Litman, B., Kim, H.Y., Gawrisch, K. (2001) Mechanisms of action of docosahexaenoic acid in the nervous system. *Lipids*, *36*, 945–959.
43. Kim, H.Y. (2007) Novel metabolism of docosahexaenoic acid in neural cells. *The Journal of Biological Chemistry*, *282*, 18661–18665.
44. Stubbs, C.D., Smith, A.D. (1984) The modification of mammalian membrane polyunsaturated fatty acid composition in relation to membrane fluidity and function. *Biochimica et Biophysica Acta*, *779*, 89–137.
45. van Echten, G., Sandhoff, K. (1993) Ganglioside metabolism. Enzymology, topology, and regulation. *The Journal of Biological Chemistry*, *268*, 5341–5344.
46. Sonnino, S., Chigorno, V. (2000) Ganglioside molecular species containing C18- and C20-sphingosine in mammalian nervous tissues and neuronal cell cultures. *Biochimica et Biophysica Acta*, *1469*, 63–77.
47. Sambasivarao, K., McCluer, R.H. (1964) Lipid components of gangliosides. *Journal of Lipid Research*, *15*, 103–108.
48. Schwarz, H.P., Kostyk, I., Marmolejo, A., Sarappa, C. (1967) Long-chain bases of brain and spinal cord of rabbits. *Journal of Neurochemistry*, *14*, 91–97.
49. Jungalwala, F.B., Hayssen, V., Pasquini, J.M., McCluer, R.H. (1979) Separation of molecular species of sphingomyelin by reversed-phase high-performance liquid chromatography. *Journal of Lipid Research*, *20*, 579–587.
50. Palestini, P., Sonnino, S., Tettamanti, G. (1991) Lack of the ganglioside molecular species containing the C20-long-chain bases in human, rat, mouse, rabbit, cat, dog, and chicken brains during prenatal life. *Journal of Neurochemistry*, *56*, 2048–2050.
51. Palestini, P., Masserini, M., Sonnino, S., Giuliani, A., Tettamanti, G. (1990) Changes in the ceramide composition of rat forebrain gangliosides with age. *Journal of Neurochemistry*, *54*, 230–235.
52. Mansson, J.E., Vanier, M.T., Svennerholm, L. (1978) Changes in the fatty acid and sphingosine composition of the major gangliosides of human brain with age. *Journal of Neurochemistry*, *30*, 273–275.
53. Kotani, M., Kawashima, I., Ozawa, H., Terashima, T., Tai, T. (1993) Differential distribution of major gangliosides in rat central nervous system detected by specific monoclonal antibodies. *Glycobiology*, *3*, 137–146.

54. Jackson, S.N., Wang, H.Y., Woods, A.S. (2005) Direct profiling of lipid distribution in brain tissue using MALDI-TOFMS. *Analytical Chemistry*, *77*, 4523–4527.

55. Hayasaka, T., et al. (2008) Matrix-assisted laser desorption/ionization quadrupole ion trap time-of-flight (MALDI-QIT-TOF)-based imaging mass spectrometry reveals a layered distribution of phospholipid molecular species in the mouse retina. *Rapid Communications in Mass Spectrometry*, *22*, 3415–3426.

56. Chen, Y., et al. (2008) Imaging MALDI mass spectrometry using an oscillating capillary nebulizer matrix coating system and its application to analysis of lipids in brain from a mouse model of Tay-Sachs/Sandhoff disease. *Analytical Chemistry*, *80*, 2780–2788.

57. Cornett, D.S., Frappier, S.L., Caprioli, R.M. (2008) MALDI-FTICR imaging mass spectrometry of drugs and metabolites in tissue. *Analytical Chemistry*, *80*, 5648–5653.

58. Jackson, S.N., et al. (2007) MALDI-ion mobility-TOFMS imaging of lipids in rat brain tissue. *Journal of Mass Spectrometry*, *42*, 1093–1098.

59. Amantonico, A., Oh, J.Y., Sobek, J., Heinemann, M., Zenobi, R. (2008) Mass spectrometric method for analyzing metabolites in yeast with single cell sensitivity. *Angewandte Chemie International Edition*, *47*, 5382–5385.

60. Burrell, M., Earnshaw, C., Clench, M. (2007) Imaging matrix assisted laser desorption ionization mass spectrometry: a technique to map plant metabolites within tissues at high spatial resolution. *Journal of Experimental Botany*, *58*, 757–763.

61. Benabdellah, F., Touboul, D., Brunelle, A., Laprevote, O. (2009) In situ primary metabolites localization on a rat brain section by chemical mass spectrometry imaging. *Analytical Chemistry*, *81*, 5557–5560.

62. Knowles, J.R. (1980) Enzyme-catalyzed phosphoryl transfer reactions. *Annual Review of Biochemistry*, *49*, 877–919.

63. Stoeckli, M., Staab, D., Schweitzer, A. (2006) Compound and metabolite distribution measured by MALDI mass spectrometric imaging in whole-body tissue sections. *International Journal of Mass Spectrometry*, *260*, 195–202.

64. Umemura, A., Mabe, H., Nagai, H., Sugino, F. (1992) Action of phospholipases A2 and C on free fatty acid release during complete ischemia in rat neocortex. Effect of phospholipase C inhibitor and N-methyl-D-aspartate antagonist. *Journal of Neurosurgery*, *76*, 648–651.

65. Rehncrona, S., Westerberg, E., Akesson, B., Siesjo, B.K. (1982) Brain cortical fatty acids and phospholipids during and following complete and severe incomplete ischemia. *Journal of Neurochemistry*, *38*, 84–93.

66. Sugiura, Y., Shimma, S., Setou, M. (2006) Thin sectioning improves the peak intensity and signal-to-noise ratio in direct tissue mass spectrometry. *Journal of the Mass Spectrometry Society of Japan*, *54*, 4.

67. Scherl, A., et al. (2005) Gold coating of non-conductive membranes before matrix-assisted laser desorption/ionization tandem mass spectrometric analysis prevents charging effect. *Rapid Communications in Mass Spectrometry*, *19*, 605–610.

68. Chaurand, P., Schwartz, S.A., Caprioli, R.M. (2002) Imaging mass spectrometry: a new tool to investigate the spatial organization of peptides and proteins in mammalian tissue sections. *Current Opinion in Chemical Biology*, *6*, 676–681.

69. Stoeckli, M., Chaurand, P., Hallahan, D.E., Caprioli, R.M. (2001) Imaging mass spectrometry: a new technology for the analysis of protein expression in mammalian tissues. *Nature Medicine*, *7*, 493–496.

70. Goodwin, R.J., Pennington, S.R., Pitt, A.R. (2008) Protein and peptides in pictures: imaging with MALDI mass spectrometry. *Proteomics*, *8*, 3785–3800.

71. Andersson, M., Groseclose, M.R., Deutch, A.Y., Caprioli, R.M. (2008) Imaging mass spectrometry of proteins and peptides: 3D volume reconstruction. *Nature Methods*, *5*, 101–108.

72. Altelaar, A.F., et al. (2006) Gold-enhanced biomolecular surface imaging of cells and tissue by SIMS and MALDI mass spectrometry. *Analytical Chemistry*, *78*, 734–742.

73. Goodwin, R.J., Dungworth, J.C., Cobb, S.R., Pitt, A.R. (2008) Time-dependent evolution of tissue markers by MALDI-MS imaging. *Proteomics*, *8*, 3801–3808.

74. Murphy, R.C., LIPID MAPS Lipidomics Workshop. (2009) Future directions: tissue and cell imaging. Available at http://www.lipidmaps.org/resources/lipidmapspresentations/EB2009/MurphyEB2009.pdf.

75. Sugiura, Y., Shimma, S., Setou, M. (2006) Two-step matrix application technique to improve ionization efficiency for matrix-assisted laser desorption/ionization in imaging mass spectrometry. *Analytical Chemistry*, *78*, 8227–8235.

76. Mock, K.K., Sutton, C.W., Cottrell, J.S. (1992) Sample immobilization protocols for matrix-assisted laser-desorption mass spectrometry. *Rapid Communications in Mass Spectrometry*, *6*, 233–238.

77. Yanagisawa, K., et al. (2003) Proteomic patterns of tumour subsets in non-small-cell lung cancer. *Lancet*, *362*, 433–439.

78. Ajiki, W., Tsukuma, H., Oshima, A. (2004) Survival rates of childhood cancer patients in Osaka, Japan. *Japanese Journal of Clinical Oncology*, *34*, 50–54.

79. Harkins, L., et al. (2002) Specific localisation of human cytomegalovirus nucleic acids and proteins in human colorectal cancer. *Lancet*, *360*, 1557–1563. Elsevier.

80. Newell, G.R., Spitz, M.R., Sider, J.G. (1989) Cancer and age. *Seminars in Oncology*, *16*, 3–9.

81. Kuriki, K., et al. (2006) Risk of colorectal cancer is linked to erythrocyte compositions of fatty acids as biomarkers for dietary intakes of fish, fat, and fatty acids. *Cancer Epidemiology, Biomarkers & Prevention*, *15*, 1791–1798.

82. Huerta, S., et al. (2003) Gene expression profile of metastatic colon cancer cells resistant to cisplatin-induced apoptosis. *International Journal of Oncology* *22*, 663–670.

83. Demirev, P.A., et al. (2002) Detection of malaria parasites in blood by laser desorption mass spectrometry. *Analytical Chemistry*, *74*, 3262–3266.

84. Rael, L.T., Ayala-Fierro, F., Bar-Or, R., Carter, D.E., Barber, D.S. (2006) Interaction of arsine with hemoglobin in arsine-induced hemolysis. *Toxicological Sciences*, *90*, 142–148.

85. Dueck, D.A., et al. (1996) The modulation of choline phosphoglyceride metabolism in human colon cancer. *Molecular and Cellular Biochemistry*, *162*, 97–103.

86. Dobrzyńska, I., Szachowicz-Petelska, B., Sulkowski, S., Figaszewski, Z. (2005) Changes in electric charge and phospholipids composition in human colorectal cancer cells. *Molecular and Cellular Biochemistry*, *276*, 113–119.

87. Brasitus, T.A., Dudeja, P.K., Dahiya, R. (1986) Premalignant alterations in the lipid composition and fluidity of colonic brush border membranes of rats administered 1, 2 dimethylhydrazine. *Journal of Clinical Investigation*, *77*, 831–840.

88. Stark, D.D., Wittenberg, J., Butch, R.J., Ferrucci, J.T. (1987) Hepatic metastases: randomized, controlled comparison of detection with MR imaging and CT. *Radiology*, *165*, 399–406.

89. Stark, D.D., et al. (1988) Superparamagnetic iron oxide: clinical application as a contrast agent for MR imaging of the liver. *Radiology*, *168*, 297–301.

90. McDonnell, L.A., et al. (2005) Subcellular imaging mass spectrometry of brain tissue. *Journal of Mass Spectrometry*, *40*, 160–168.

91. Chaurand, P., et al. (2004) Integrating histology and imaging mass spectrometry. *Analytical Chemistry*, *76*, 1145–1155.

92. Astigarraga, E., Barreda-Gómez, G., Lombardero, L., Fresnedo, O., Castaño, F., et al. (2008) Profiling and imaging of lipids on brain and liver tissue by matrix-assisted laser desorption/ionization mass spectrometry using 2-mercaptobenzothiazole as a matrix. *Analytical Chemistry*, *80*, 9105–9114.

93. Sugiura, Y., Shimma, S., Konishi, Y., Yamada, M.K., Setou, M. (2008) Imaging mass spectrometry technology and application on ganglioside study: visualization of age-dependent accumulation of C20-ganglioside molecular species in the mouse hippocampus. *PLoS ONE*, *3*, e3232.

94. Ageta, H., Asai, S., Sugiura, Y., Goto-Inoue, N., Zaima, N., Setou, M. (2009) Layer-specific sulfatide localization in rat hippocampus middle molecular layer is revealed by nanoparticle-assisted laser desorption/ionization imaging mass spectrometry. *Medical Molecular Morphology*, *42*, 16–23.

95. Cha, S., Yeung, E.S. (2007) Colloidal graphite-assisted laser desorption/ionization mass spectrometry and MSn of small molecules. 1. Imaging of cerebrosides directly from rat brain tissue. *Analytical Chemistry*, *79*, 2373–2385.

96. Zhang, H., Cha, S., Yeung, E.S., (2007) Colloidal graphite-assisted laser desorption/ionization MS and MS(n) of small molecules. 2. Direct profiling and MS imaging of small metabolites from fruits. *Analytical Chemistry*, *79*, 6575–6584.

Chapter 4

Imaging Mass Spectrometry: Sample Preparation, Instrumentation, and Applications

Kamlesh Shrivas[†,‡] and **Mitsutoshi Setou**[†]

Contents

[†] Department of Cell Biology and Anatomy, Hamamatsu University School of Medicine, 1-20-1 Handayama, Higashi-Ku, Hamamatsu, Shizuoka 431-3192, Japan
[‡] Department of Chemistry, Guru Ghasidas University, Bilaspur-495009, CG, India

Advances in Imaging and Electron Physics, Volume 171, ISSN 1076-5670, DOI: 10.1016/B978-0-12-394297-5.00004-0.

1. INTRODUCTION

The ability to visualize the molecular distribution in biological material such as tissue samples has helped scientists to provide a better understanding of the principles of life. The study of biomolecule distribution in organs and its alterations with disease remains one of the most challenging and intriguing scientific issues of recent times. Various techniques are used in laboratories around the world to visualize molecular systems—techniques such as magnetic resonance imaging (MRI) technology (Hurd and Freeman, 1989) and positron electron tomography (PET) (Ametamey *et al.*, 2008). The Nobel Prize–winning MRI and PET technologies are known as noninvasive techniques for medical diagnosis. Nuclear magnetic resonance spectroscopy (NMRS) is also helpful for imaging and identification of biomolcules in tissue sample (Hiltunen *et al.*, 2002). The limitations of these techniques are the relatively poor resolution, sensitivity, and requirement of labeling of molecules for detection (in the case of the PET method).

Imaging mass spectrometry (IMS) was introduced for spatial distribution analysis of biomolecules without the need for extraction, purification, separation, or labeling of biological samples. Recent developments in molecular imaging have created new opportunities to perform molecular diagnostic and therapeutic procedures. The technique can be exploited to visualize cellular and molecular processes that occur in two-dimensional (2D) or three-dimensional (3D) fashion without perturbing the structure of the system (Caprioli *et al.*, 1997; Setou *et al.*, 2010).

Mass spectrometry (MS) is a technique based on the measurement of the charged ions in an electric or magnetic field. Generally, a mass spectrometer contains three distinct parts: (1) an ion source producing ions from sample molecules; (2) a mass analyzer separating the different molecules with respect to their mass-to-charge ratios (m/z), and (3) a detector, registering the ion m/z and the intensity at which the ions were detected. Data are collected and visualized in a mass spectrum where the different m/z ratios are displayed as a function of their signal intensity (Gross, 2004). MS is a great scientific tool because of the wide range of molecules that can be accurately detected and identified: large organic compounds and biomolecules of low molecular weight.

In the beginning, mass spectrometric analysis was limited to samples that had undergone excessive preparation procedures, such as purification, separation, and concentration steps. These procedures not only jeopardize sample integrity, but also lead to the complete loss of any spatial distribution information. MS instruments are equipped with different ionization methods, including electron ionization and chemical ionization (Fales *et al.*, 1972), fast atomic bombardment (Morris *et al.*, 1981), electrospray ionization (ESI) (Fenn *et al.*, 1989), and matrix-assisted laser desorption/ionization (MALDI) (Karas *et al.*, 1985) for the analysis of a wide range of organic and bio-organic molecules. The introduction of the "soft" ionization sources such as ESI and MALDI transfigured MS, as it offered the capability to analyze large intact biomolecules.

At present, IMS is a well-recognized technique for profiling the distribution of biomolecules in tissue sample at micrometer to nanometer resolution (Caprioli *et al.*, 1997; Goodwin *et al.*, 2008; McDonnell and Heeren, 2007; Pol *et al.*, 2010; Shimma *et al.*, 2008). Data acquisition is performed through scanning a tissue section with a laser, thereby obtaining one mass spectrum for every pixel. The main principle of IMS is based on desorption and ionization of biomolecules from the surface of the tissue sample. There are currently four important desorption/ionization methods: desorption electrospray ionization (DESI) (Takats *et al.*, 2004), secondary ion mass spectrometry (SIMS) (Benninghoven, 1973), MALDI (Tanaka *et al.*, 1988) and laser ablation electrospray ionization (LAESI) (Nemes and Vertes, 2007).

2. IONIZATION METHODS FOR IMAGING MASS SPECTROMETRY

2.1. Desorption Electrospray Ionization

DESI was introduced by R.G. Cooks in 2004. In DESI, the molecules are ionized at atmospheric pressure without the use of any organic matrix (Dill *et al.*, 2009) in a combination of ESI and desorption ionization (DI). The charged droplets of solvent generated during the electrospray stage are used to ionize molecules from the surface of the sample and the ions produced thereby are directed into an atmospheric inlet of the MS. The components and use of DESI in IMS are presented in Figure 1a. The spatial resolution obtained by this method is 0.3–0.5 mm, which is a low resolution of tissue sample in IMS studies. DESI has been successfully applied to IMS for the identification of lipids, drug metabolites, and antifungal molecules in seaweeds (Dill *et al.*, 2009; Lane *et al.*, 2009; Wiseman *et al.*, 2008).

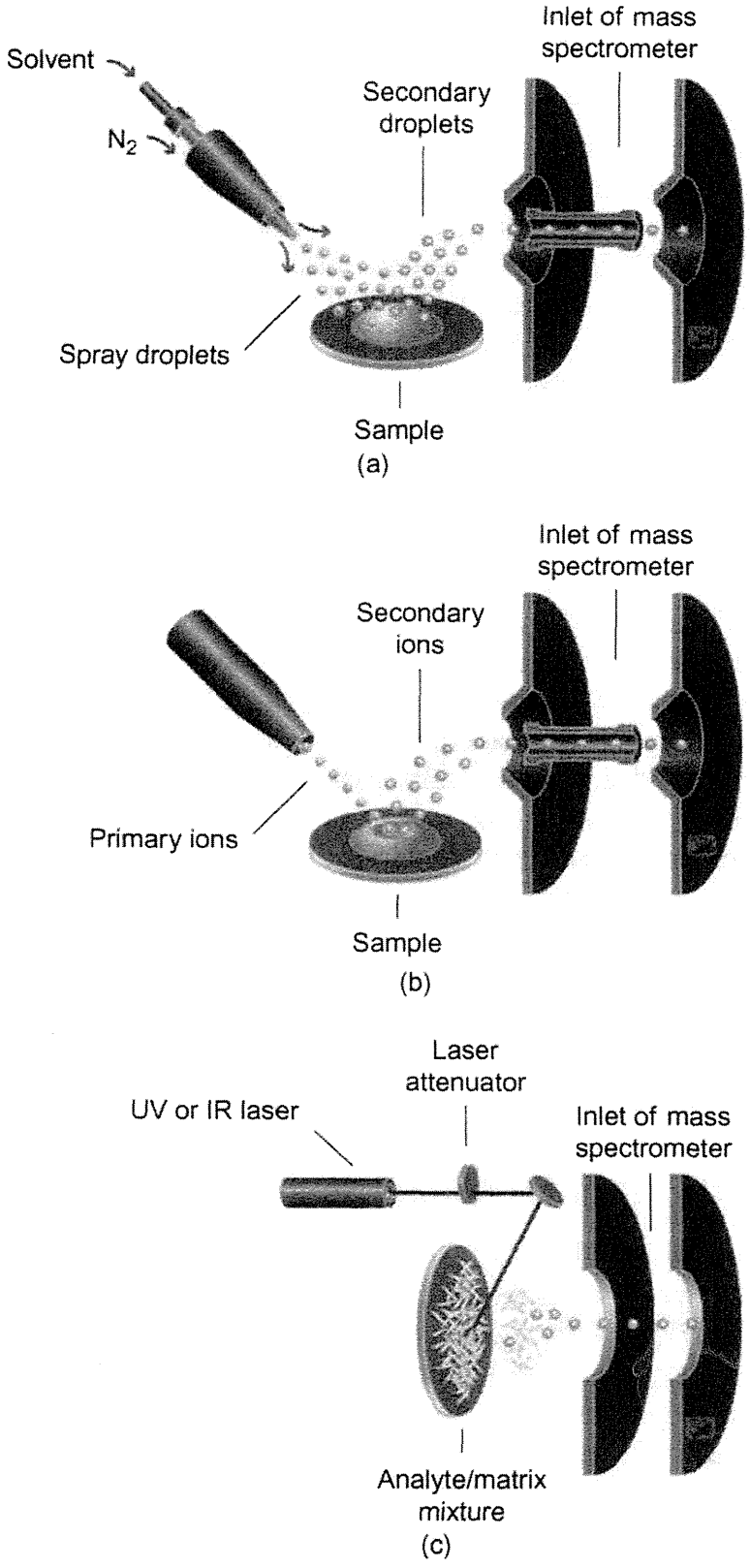

FIGURE 1 Desorption-ionization techniques used in mass spectrometry imaging. (a) Desorption electrospray ionization (DESI). (b) Secondary ion mass spectrometry (SIMS). (c) Matrix-assisted laser desorption ionization (MALDI). UV, ultraviolet; IR, infrared. Reprinted from Pol *et al.* (2010) with permission from Springer. (See Color Insert.)

2.2. Secondary Imaging Mass Spectrometry

SIMS is a sophisticated technique that uses ion beams from metal ions such as Ar^+, Ga^+, and In^+ (here denoted *primary ion beams*) to produce secondary ions from molecules on the surface of a sample. Ionization is performed in high vacuum to avoid a collision with surrounding gas molecules, and the primary ion beams can be focused down to 50 nm on the sample surface, with the resolution depending on the current and charge state of the ions. SIMS coupled with time-of-flight (TOF-SIMS) is a superior tool for high-spatial, submicron resolution (< 10 nm). Thus SIMS can be applied for the differentiation of biomolecules that are present all the way down to the cellular level. However, fragmentation of larger molecules on the sample surface is observed when strong laser energy is applied for the primary ion beam. Hence, SIMS is primarily applicable for the analysis of small molecules (< 1000 Da) (Heeren *et al.*, 2006; Slaveykova *et al.*, 2009). Figure 1b shows the process of SIMS ionization of molecules from the sample surface. SIMS has been applied for imaging of samples such as single cells, embryos, brain, cocaine, and cinnamoylcocaine in coca (Colliver *et al.*, 1997; Jones *et al.*, 2007; Wu *et al.*, 2007). The fragmentation of molecules in SIMS can be overcome through the treatment of an organic MALDI matrix; this approach is known as matrix-enhanced (ME)-SIMS (Altelaar *et al.*, 2007).

2.3. Laser Ablation Electrospray Ionization

LAESI was developed by Nemes and Vertes (2007) and is a method for MS analysis of tissue samples without sample preparation under atmospheric pressure (Nemes and Vertes, 2007). Laser ablation from a mid-infrared (mid-IR) laser is combined with a secondary ESI process. The spatial resolution for tissue samples using LAESI technique is better than DESI and can be used for imaging of biomolecules from the surface of tissue sample at a lateral resolution of < 200 μm. The technique has been applied for imaging and identification of plants, tissues, cell pellets, and even single cells (Nemes *et al.*, 2010; Shrestha *et al.*, 2010; Sripadi *et al.*, 2010). Recently it has also been used in 3D imaging of molecules from the sample (Nemes *et al.*, 2009).

2.4. Matrix-Assisted Laser Desorption/Ionization

MALDI was introduced as a soft ionization technique that causes little or no fragmentation of the target molecules, allowing for the analysis of molecules at several hundred kilodaltons (i.e., high m/z values). This allows for mass spectrometric analysis of a wide range of molecules such as amino acids, peptides and proteins, carbohydrates, and nucleic acids and drugs and has proven to be one of the most powerful MS technologies